

UC San Diego

UC San Diego Previously Published Works

Title

Stretchable Dry Electrodes with Concentric Ring Geometry for Enhancing Spatial Resolution in Electrophysiology

Permalink

<https://escholarship.org/uc/item/16p843tt>

Journal

Advanced Healthcare Materials, 6(19)

ISSN

2192-2640

Authors

Wang, Kaiping
Parekh, Udit
Pailla, Tejaswy
et al.

Publication Date

2017-10-01

DOI

10.1002/adhm.201700552

Peer reviewed

Stretchable Dry Electrodes with Concentric Ring Geometry for Enhancing Spatial Resolution in Electrophysiology

Kaiping Wang, Udit Parekh, Tejaswy Pailla, Harinath Garudadri, Vikash Gilja, and Tse Nga Ng*

The multichannel concentric-ring electrodes are stencil printed on stretchable elastomers modified to improve adhesion to skin and minimize motion artifacts for electrophysiological recordings of electroencephalography, electromyography, and electrocardiography. These dry electrodes with a poly(3,4-ethylenedioxythiophene) polystyrene sulfonate interface layer are optimized to show lower noise level than that of commercial gel disc electrodes. The concentric ring geometry enables Laplacian filtering to pinpoint the bioelectric potential source with spatial resolution determined by the ring distance. This work shows a new fabrication approach to integrate and create designs that enhance spatial resolution for high-quality electrophysiology monitoring devices.

Measurement of electrophysiological signals is crucial for monitoring bodily states and facilitating clinical diagnosis of diseases. Electrophysiological recordings such as electroencephalography (EEG), electromyography (EMG), and electrocardiography (ECG) are routinely done using arrays of electrodes that measure local electrical activities.^[1–3] Spatial information is important in EEG to localize active brain regions and in EMG to measure neuromuscular activity. In ECG, the progression of cardiac depolarization signals can be tracked using 12 leads located on the torso to diagnose various cardiac abnormalities, such as arrhythmias and infarctions. However, the spatial resolution of an electrode array is affected by the blurring effects from different conductivities of the torso volume and modified electrode designs^[4,5] are shown to be more effective for increasing spatial resolution than merely increasing the number of electrodes in an array. In addition, conventional gel electrode arrays are limited by the complexity of electrode placement, which is laborious, time consuming, and only transiently useful since performance degrades once the gel dries. Thus, to enhance the spatial resolution and reliability of electrophysiology studies while reducing setup complexity, this paper demonstrates a dry concentric ring electrode design through an

additive printing process^[6–11] that allows rapid reconfiguration and integration of multichannel electrodes.

The concentric ring design is a physical approximation to the Laplacian filter, which is the second spatial derivative of the measured potentials and essentially assigns more weight to changes in bioelectric dipoles under measurement points, to enable better differentiation between concurrent, closely spaced dipole sources.^[12,13] While the Laplacian filter may be applied through computation on arrays consisting of discrete five-point or nine-point electrodes, the concentric ring approximation in **Figure 1** simplifies orientation prob-

lems and significantly reduces the number of electrodes. Previously, concentric ring electrodes were demonstrated with silver or gold as the conductor interfacing with the human body. However, the metallic interfaces have high impedance and usually require a thin layer of conductive gel, which smears the spatial resolution and may also short the electrode rings if the gel bridges them. Thus practical implementation of the Laplacian filter requires a dry interface,^[14–16] which requires further materials and device development to match the signal-to-noise (SNR) level of standard gel electrodes.

The work in this paper takes advantage of the recent advances in the use of conducting polymer^[17–20] as dry electrode interface. The conducting polymer poly(3,4-ethylenedioxythiophene) polystyrene sulfonate (PEDOT:PSS) has enabled a better interface with skin because of the mixed ionic/electronic conductivity^[21] and biocompatibility^[22] of PEDOT:PSS. Moreover, the dry electrodes here are patterned on stretchable elastomers modified to improve adhesion to skin^[23] and minimize motion artifacts. We use a simple stencil-printing technique to directly deposit silver/silver chloride (Ag/AgCl) and PEDOT:PSS on modified polydimethylsiloxane (PDMS) elastomer, to create customizable, wearable devices at low cost. The dry, multichannel concentric ring electrodes are shown to outperform commercial gel electrodes in providing consistent high-quality signals for EEG and ECG, and with good spatial contrast at ring diameter of 6 mm for EMG measurement.

Our choice of substrate is a moldable elastomer consisting of PDMS with a trace amount of ethoxylated polyethylenimine (PEIE), which modifies the crosslinking network to reduce the Young's modulus and roughen the substrate surface.^[23] The substrate is semitransparent, due to optical scattering by the micrometer-sized wrinkles on the surface.

K. Wang, U. Parekh, T. Pailla, Dr. H. Garudadri, Dr. V. Gilja, Dr. T. N. Ng
Department of Electrical and Computer Engineering
University of California San Diego
9500 Gilman Drive, La Jolla, CA 92093-0407, USA
E-mail: tnn046@ucsd.edu

 The ORCID identification number(s) for the author(s) of this article can be found under <https://doi.org/10.1002/adhm.201700552>.

DOI: 10.1002/adhm.201700552

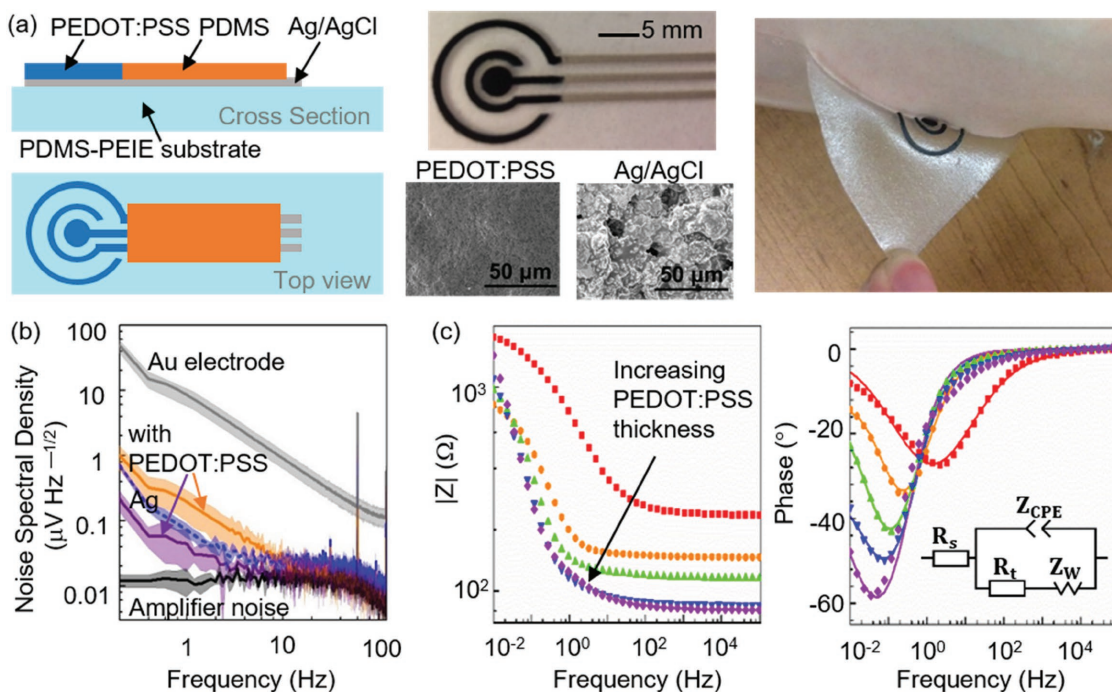


Figure 1. a) Schematic and photograph of a concentric ring electrode patterned by stencil printing. The scanning electron microscopy images show the surface morphology of a typical electrode covered with PEDOT:PSS or with bare Ag/AgCl. The printed dry electrode adheres well to skin as shown in the right photograph. b) Noise power spectral density of various electrodes. Error bars were indicated by the shaded area and calculated from averaging over a sampling period of 90 s. Gray line: commercial gold electrode. Orange line: printed electrode where the PEDOT:PSS thickness is 2.8 μm . Blue dashed line: commercial Ag/AgCl with hydrogel (3M part T716). Purple line: printed electrode where the PEDOT:PSS thickness is 9.9 μm . Black line: amplifier noise. c) Impedance magnitude and phase angle of the printed electrodes. The thickness of PEDOT:PSS layer is 0 μm (red, bare Ag/AgCl), 2.8 μm (orange), 4.5 μm (green), 6.8 μm (blue), and 9.9 μm (purple). The error bars for the film thicknesses are provided in Table 1. The inset shows the equivalent circuit model used for parameter fittings (solid lines).

The micrometer-sized wrinkles on the PDMS-PEIE elastomer enhance van der Waals forces and increases the adhesion force to skin (Figure 1). The strong adhesion allows the electrodes printed on this substrate to be securely fastened to the skin and maintain good electrical contact without conductive gel.

The concentric ring electrode design in Figure 1a was patterned through a laser-cut stencil mask, and the geometry was based on the nine-point Laplacian estimation method^[24] (Figure S1, Supporting Information), which in our design was scaled to probe a dipole depth of ≈ 1 cm beneath the electrode surface. The diameter of the central disc was 4 mm. The inner diameter of the middle ring and the outermost ring was 6 and 14 mm, respectively, both with a linewidth of 1 mm. The Ag/AgCl traces were deposited to form highly conductive interconnects with the resistivity of 500 $\mu\Omega$ cm. In the concentric ring region, the Ag/AgCl was covered with PEDOT:PSS to further lower the electrode impedance. Figure 1b compares the voltage noise of our PEDOT:PSS-covered electrodes to commercially available Au and Ag/AgCl electrodes with hydrogel from 3M. The electrode impedance was measured through a conductive gel, which was a uniform electrolyte on top of the pair of electrodes. Since the power spectral density^[25,26] S_N of voltage noise v_N is inversely proportional to square root of the electrode area A by $S_N = v_N/A^{0.5}$, in Figure 1b the noise spectra of the 3M electrode and the printed electrodes are scaled by area for comparison to the Au electrode with a diameter of 1 cm. The electrode diameters were 1.5 cm for the 3M electrode and 0.8 cm

for the printed electrodes, which were made in disc shapes and not concentric rings to facilitate comparison. Among the various electrodes including commercial ones, our printed electrode with a 9.9 μm PEDOT:PSS layer shows the lowest noise voltage across the spectrum.

The excellent noise level of the printed electrodes is attributed to the low interfacial impedance of the organic PEDOT:PSS conductor. Noting the reduction in noise voltage with a thick PEDOT:PSS layer, we varied the PEDOT:PSS thickness and measured the electrode impedance by electrochemical impedance spectroscopy. In Figure 1c the impedance of bare Ag/AgCl electrode is at least two times higher than the ones with PEDOT:PSS. As the PEDOT:PSS film thickness is increased from 2.8 to 9.9 μm , the impedance phase reveals a transition to higher capacitance at low frequency. The impedance magnitude for electrodes with 6.8 and 9.9 μm PEDOT:PSS is very similar for frequencies above 0.1 Hz, indicating that further increase beyond 9.9 μm is not necessary for impedance reduction and hence the printed electrodes for electrophysiological recordings were fabricated with PEDOT:PSS film with thicknesses ranging from 7 to 9 μm .

The electrode impedance characteristics were analyzed by fitting to the equivalent circuit model^[27,28] in the inset of Figure 1c, where R_s is the series resistance, R_t is the charge transfer resistance, Z_{CPE} is the constant phase element, and Z_w is the semi-infinite Warburg diffusion element related to ion movement in PEDOT:PSS. The fit results are summarized in Table 1 and

Table 1. Fit values to the equivalent circuit model for the printed electrodes.

PEDOT:PSS thickness [μm]	R_s [Ω]	R_t [Ω]	Q [mF s^{n-1}]	n	R_w [$\Omega\text{s}^{-1/2}$]
Bare Ag/AgCl	235	1636	0.47	0.60	–
2.8 ± 0.3	148	623	2.50	0.82	28
4.5 ± 0.5	119	916	4.13	0.84	33
6.7 ± 0.8	89	1000	5.16	0.85	117
9.9 ± 1.0	87	1788	6.06	0.88	151

the fitted plots are provided in Figure S2 (Supporting Information). The constant phase element^[29] accounts for nonidealities in capacitance and is expressed by $Z_{\text{CPE}} = \frac{1}{Q}(j \cdot \omega)^{-n}$, where $j = \sqrt{-1}$, $0 < n < 1$, ω is radial frequency, and Q is a constant with the dimension of farads multiplied by seconds to the power of $(n - 1)$. If $n = 1$, the expression is reduced to the case of an ideal capacitor. The exponent n is affected by roughness or porosity, which explains the lower n value for the rough Ag/AgCl surface as seen in Figure 1a. The Warburg diffusion element is expressed by $Z_w = R_w/\sqrt{\omega} + R_w/(j \cdot \sqrt{\omega})$, where R_w is the Warburg resistance, ω_0 is a characteristic radial frequency. In our case Z_w is essentially negligible to electrophysiological measurement as it affects the impedance only at very low frequency range < 0.5 Hz.

With increasing PEDOT:PSS thickness, the electrode series resistance is reduced. The charge-transfer resistance, along with the constant phase element, increases and indicates capacitive characteristics becoming more dominant with thicker PEDOT:PSS films. The current measured by impedance spectroscopy consists of two components, where the Faradaic contribution is caused by electrochemical reaction on the electrode surface, and the non-Faradaic component is due to charging of the double-layer capacitance at the electrode–electrolyte interface. As the charge-transfer resistance increases, there is less

Faradaic contribution. Meanwhile, the non-Faradaic component increases because thicker PEDOT:PSS films are still permeable^[21] to ions and larger surface areas enhance the electric double layer effect at low frequencies. Overall, the low interface impedance of the printed electrodes is suitable for biosignal detection, since lower impedance would translate to higher SNR. In addition, the large capacitance is also advantageous if the electrodes are to be used for electrostimulation.

The change in conductor resistance was examined as the elastomeric substrate was stretched uniaxially along the length of printed lines with linewidth of 0.8 mm and thickness of 30 μm . The conductor samples in Figure 2 were straight lines for the purpose of determining the stretchability limit of the printed Ag/AgCl blended with 6% elastomer. Higher tolerance to strain would be achieved if the conductor traces were designed with other patterns such as serpentine or fractals. The fabrication process here will be adaptable for implementing these geometries if an increase in strain tolerance is needed. Without any geometric optimization, the printed Ag/AgCl interconnect remained conductive up to 30% strain, which met the requirement for tolerating the chest volume expansion during breathing. The Ag/AgCl line was cracked and became open at 36.7% strain. The Ag/AgCl trace resistance R increased up to sevenfold from 0% to 30% strain, and the resistance recovered to the original value R_0 upon release (Figure S3, Supporting Information). For the conductor line where 9 μm of PEDOT:PSS was coated on top of the Ag/AgCl, the resistance change with stretching was higher than the line without the coating because the PEDOT:PSS layer showed cracks by 15% strain. Therefore, we confined the PEDOT:PSS coating to the electrode areas for recordings and left the rest of the interconnect traces as Ag/AgCl to minimize resistance change with stretching.

The electrodes on PEIE-modified PDMS substrate adhered to skin by van der Waals force, allowing the electrodes to be deployed without conductive gel and adhesives that may be irritating for long-term wear. Stretching may initiate delamination

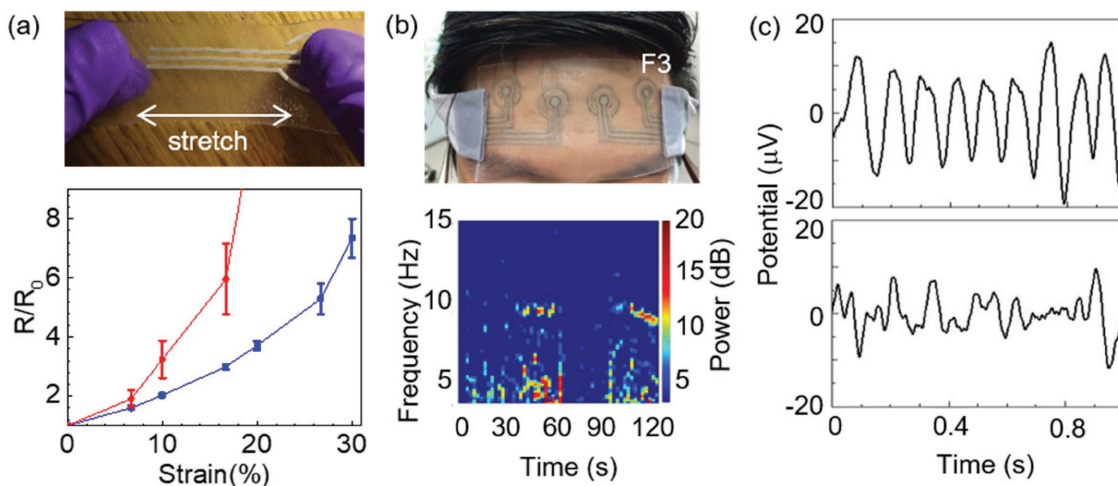


Figure 2. a) Photograph of printed lines being stretched linearly to 30% strain, and the change in resistance of linear conductor traces under uniaxial stretching. Ag/AgCl blended with 6% elastomer, with 9 μm PEDOT:PSS coating (red) and without coating (blue). b) Photograph of the printed dry electrodes incorporated into one headband. EEG spectrogram of alpha rhythm oscillations recorded by the dry electrode at F3 position according to the 10–20 system. c) Time traces of the EEG recording during the period with (top) and without (bottom) alpha rhythm oscillations.

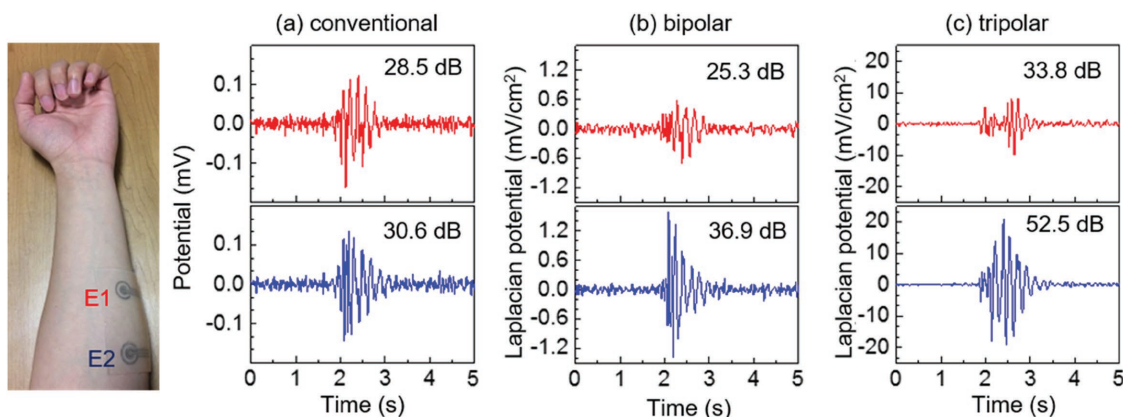


Figure 3. Photograph of the dry electrode locations in EMG recordings. The EMG signals measured a) conventionally or with Laplacian filtering in b) bipolar or c) tripolar configuration. The SNR values are listed in the upper right corner of each plot.

at the edge of the substrate, but prior work^[30] has shown that the delamination would be mitigated by decreasing the substrate thickness. The substrate stayed in place for several hours (tested up to 4 h) during light activities such as walking or carrying out EMG movement tasks.

The dry electrodes can be integrated into one band to incorporate multiple measurement channels. In Figure 2b, our substrate was connected to a stretchable textile to put the whole device under tension to keep the headband in place. We had placed a band of printed electrodes on a volunteer's forehead to measure alpha rhythm oscillations, which are prominent 10 Hz signals shown in the EEG spectrogram. The oscillations were detected when the person closed his eyes and gathered his concentration; otherwise, the signal disappeared, for example between 0–30 and 60–90 s in Figure 2b. The alpha rhythm oscillations occurred in the occipital lobe far from forehead where the electrodes were located. Since the alpha rhythm signals were not localized at the forehead, there was no significant difference between the recordings of the left and right electrodes on the band. However, in EMG and ECG measurement below, the spatial resolution of the signals was enhanced and local signals were differentiated by the concentric ring electrodes.

The concentric ring electrodes were configured to take differential measurement between the middle ring and the central electrode and also between the outer ring and the central electrode. The same electrodes were used as conventional “disc” electrodes by taking measurement with only the central electrode, with respect to a reference electrode placed at locations at which negligible EMG activity is expected, for example at the bony part of the volunteer's wrist for EMG.

With the electrode design in Figure 1a, there were two options to apply the Laplacian filter, namely the bipolar and tripolar configurations.^[12] The bipolar configuration used the five-point approximation commonly used for edge detection; the bipolar Laplacian potential was the difference between the outer ring and the central electrode, with respect to the area inside the outer ring. The tripolar configuration extended the filter to the nine-point approximation to increase localization, with a tradeoff in adding complexity with an additional middle ring (Figure S1, Supporting Information). The approximation expressions^[12] for the two cases are

$$\text{Bipolar Laplacian potential: } L_{Bp} = \frac{4}{(2r)^2} (V_O - V_D) \quad (1)$$

$$\text{Tripolar Laplacian potential: } L_{Tp} = \frac{1}{3r^2} [16(V_M - V_D) - (V_O - V_D)] \quad (2)$$

where V_D , V_M , and V_O are the potential measured from the inner disc, the middle ring, and the outer ring of an electrode, respectively, and r is the distance between the center of disc and middle ring. In our design the spacing between the center of disc and outer ring is $2r$. The measured potential difference $V_O - V_D$ and $V_M - V_D$, before the calculation of Laplacian spatial derivatives, are included in Figure S4 (Supporting Information).

The EMG measurement in Figure 3 compares the signals obtained from two dry electrodes placed 45 mm apart on the forearm of a volunteer. As the volunteer clenched his hand into a fist, neuromuscular potential was detected by both electrodes. Using the conventional measurement technique, the two electrodes simultaneously recorded very similar signals in Figure 3a, and as such implied that the spatial resolution was very low and the signals were practically indistinguishable at distance <45 mm. Upon changing to the Laplacian differential method, in which the signals at the concentric rings were measured with respect to the central disc, the EMG signal at the location of electrode E2 is shown in Figure 3b,c to be stronger than at location E1, since E2 is closer to the neuromuscular potential source that activated the clenching movement. The Laplacian measurement distinguished the signal source location, offering better spatial resolution than the approach based on comparing potentials of discrete electrodes.

The signal-to-noise ratio for the bipolar and tripolar EMG signal was calculated by the equation $SNR = 20 * \log \sqrt{\sum_i Sf_i^2 / \sum_i (Sr_i - Sf_i)^2}$, where Sr is the raw signal and Sf is the filtered signal. The SNR from the tripolar configuration is higher than that of the bipolar one in Figure 3 with respect to an equivalent area of $\pi(2r)^2$. If the bipolar Laplacian potential is measured with respect to πr^2 , the SNR at

the E2 location increases to 51.2 dB as seen in the Figure S4 (Supporting Information) because the signal is localized within the area within the middle ring. Overall the signals were distinguishable at the spatial resolution of $r = 6$ mm, corresponding to the distance between the middle ring and the disc center of the printed electrode. The signal from the concentric ring electrode is compared to the pair of conventional “disc” electrodes in Figure 3a with the same sensing area. This spatial contrast of 6 mm from using concentric rings is much better than the previous limit from using disc electrodes in Figure 3a, where signals at 45 mm apart were hardly distinguishable.

For ECG, we used our dry concentric ring electrodes to measure the potential difference $V_O - V_D$ (in units of μV) for comparison with signals from the standard 12-lead measurement. There was no significant difference in signals of $V_O - V_D$ and $V_M - V_D$ (shown in Figure S4, Supporting Information), since the distance between the concentric rings used here is small ($r = 6$ mm) in relation to cardiac physiology. Here we did not compute Laplacian potentials (in units of $\mu\text{V cm}^{-2}$) because typical ECG analysis does not require spatial derivatives.

The visualization of the PQRST peaks is very important for clinical diagnosis. It is especially challenging to identify P peaks as they are the lowest of the ECG waves. P-waves provide clues to atrial activities, but the signals are weak because there are fewer cardiac cells involved in atrial activation than in other ventricular activities. In Figure 4a, the Lead-I signal was measured by monopolar commercial gel electrodes connected to the limbs. Conventional Lead-I results typically show the highest P-waves when compared to measurement at V_1 position,^[13] but the limb positions are inconvenient for movement. The signal in Figure 4b was taken at a convenient core position with the compact dry electrode. This signal $V_O - V_D$ from concentric ring electrodes was small because the distance between the outer rings and the central disc was much shorter than the distance across the arm span (>1 m) between the Lead-I electrode and its reference electrode. Nevertheless, in terms of the P-wave

amplitude with respect to the full ECG peak-to-peak amplitude, the signal in Figure 4b provided similar P-wave contrast. Whereas the P-wave was at 13% for the Lead-I signal normalized by a peak-to-peak amplitude of 342 μV , the P-wave was at 18% for the Figure 4b signal normalized by 34 μV . Hence, after amplitude normalization, the signals obtained by concentric ring electrodes maintain good contrast for identifying P-waves associated with atrial activity. The compact concentric ring configuration is reliable and comparable to the conventional limb leads and provides an additional advantage of eliminating dangling wire connections that impede mobile monitoring.

In conclusion, we demonstrate printed dry electrodes on stretchable substrates that are moldable to conform and provide good adhesion to skin for electrophysiological recordings of EEG, EMG, and ECG. These electrodes with a PEDOT:PSS interface layer are optimized to a thickness that shows lower noise level than that of commercial gel electrodes. The concentric ring geometry enables Laplacian filtering to pinpoint the bioelectric potential source with spatial resolution determined by the ring distance. The EMG and ECG recordings show enhanced localization of signal sources and the measurement using concentric ring electrodes provides significant advantage in being much more simple and easy to set up compared to using multiple discrete electrodes to extract Laplacian potentials. This work shows a new fabrication approach to integrate and create designs that enhance spatial resolution for high-quality electrophysiology monitoring devices at low cost.

Experimental Section

Electrode Fabrication: The substrate was comprised of PDMS (Sylgard 184, Dow Corning) modified with PEIE (80% ethoxylated polyethylenimine solution, Sigma-Aldrich) to tune the mechanical compliance and adhesive properties of the PDMS elastomer. The PDMS base and crosslinking agent were mixed at 10:1 ratio by weight; for 10 g of the mixture, 35 μL of PEIE was added to induce a heterogeneous

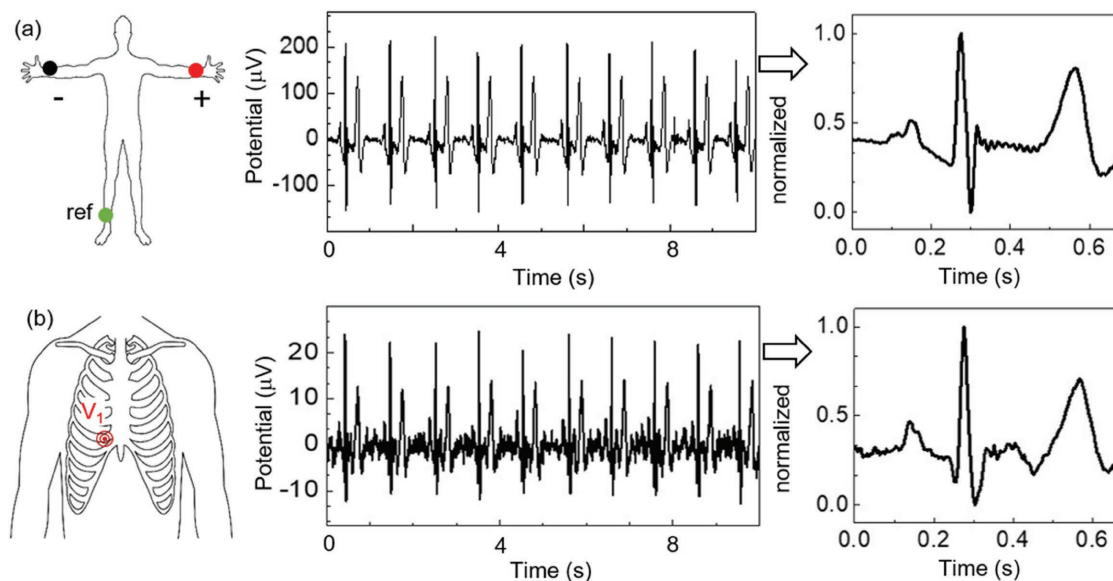


Figure 4. ECG electrode locations are indicated by the cartoon schematics. a) Signal of Lead-I based on the standard 12-lead protocol. b) Signal measured by dry concentric ring electrodes at the core V_1 location.

crosslinking network.^[23] The mixture was degassed and poured into a mold to cure at 90 °C for 3 h to obtain a substrate with typical thickness of 2 mm.

To form electrodes, conductive inks were spread with a wire-wound rod through a stencil mask (Metal Etch Services, San Marcos, CA) onto the cured substrate. Silver/silver chloride ink (E2414, Ecron) was mixed with Ecoflex-50 (Smooth On) at 94:6 weight ratio to increase the conductor stretchability.^[31] The Ag/AgCl ink was annealed at 90 °C for 5 min and the typical trace thickness was 30 μm. Subsequently, PEDOT:PSS (for screen printing, Sigma-Aldrich) was printed through another stencil mask to cover the Ag/AgCl in the concentric ring region. The PEDOT:PSS formulation was 1 g of PEDOT:PSS with 0.4 mL of ethylene glycol, 5 μL of 4-dodecylbenzenesulfonic acid as a surfactant, and 40 mg 3-glycidoxypropyltrimethoxysilane as a crosslinker. By printing multiple passes, the thickness of PEDOT:PSS was adjusted from 2.8 to 9.9 μm. The thickness of PEDOT:PSS was measured by Alpha Step 200 Profiler at a scan rate of 50 μm s⁻¹. In between printing passes, each layer was annealed at 100 °C for 20 min. A layer of PDMS is used to encapsulate and isolate the Ag/AgCl interconnects from the skin. Currently thin wires are embedded in the elastomer substrate to make connections between the printed electrodes and the amplifier board, but in the future wireless communication chips may be embedded in the substrate to eliminate the dangling wires.

Electrode Characterization: To measure the noise spectrum, each pair of test electrodes were placed side by side, with the active areas in contact with ≈1 mm thick layer of conductive gel (Ten20, Weaver) connecting the two electrodes. Voltage noise between the electrode pair was measured by an OpenBCI board (Cyton biosensing board Kit, OpenBCI) set to an amplifier gain of 24. The reported noise was an average over 90 s at a sampling rate of 250 Hz. The background noise of the board amplifier was measured by shorting the two inputs. The time-domain voltage data were Fourier transformed with no additional signal filtering. The peaks at 30 and 60 Hz are due to power line noise.

The electrochemical impedance spectroscopy was taken with a potentiostat (Bio-Logic SP-200) in a two-electrode configuration supplying a sinusoidal signal of 10 mV without any dc bias. The electrode impedance was measured through a conductive gel, which was a uniform electrolyte sandwiched between the electrodes. Each electrode had an area of 0.5 cm². The impedance between the electrode–skin interface is compared for different electrodes (Figure S5, Supporting Information) and monitored over one hour (Figure S6, Supporting Information). The Bio-Logic software EC-Lab was used for the equivalent circuit model fittings.

The noise power spectra of a dry electrode with 9.9 μm PEDOT:PSS coating under 10% and 20% uniaxial stretching are shown in Figure S7 (Supporting Information). The measurement was done by connecting the electrodes through conductive gel. Two ends of the electrode substrate were attached to the two sides of a drill press vise by tape. The gap between the two vise plates was adjusted by manually turning the screw to stretch the substrate.

In Vivo Recordings: A volunteer provided signed consent to participate in this study. The electrodes were connected to the OpenBCI board set to an amplifier gain of 24 sampled at 250 Hz. The sites for electrode attachment were swiped with 70% ethanol.

The EEG alpha rhythm oscillations were measured by placing the recording electrode on the left frontal area, at the F3 position in the standard 10–20 system. The reference and ground electrodes were attached at the two ear lobes, which are the A1 and A2 positions in the 10–20 system. The recording and reference electrodes were our dry electrodes directly adhered to the skin. For convenience with wiring, the ground electrode was a commercial gold electrode with conductive gel. To measure the alpha rhythm oscillations, the volunteer was asked to alternately open and close his eyes for 30 s periods. For control comparison, the time traces of the alpha rhythm oscillations recorded with commercial Au electrodes at F3 position are shown in Figure S8 (Supporting Information). The EEG signals were digitally filtered in MATLAB by a sixth-order Butterworth filter with a range of 1–40 Hz.

For EMG recordings, the volunteer was stationary and placed his left elbow on a desk. The reference electrode and the recording electrodes were our dry electrodes directly placed on the forearm. The volunteer was asked to clench his hand into a fist as EMG signals at E1 and E2 locations were simultaneously recorded by the OpenBCI board. The EMG signals were digitally filtered in MATLAB by a sixth-order Butterworth filter with a range of 5–40 Hz.

For ECG recordings on the chest of a volunteer lying in supine position, the dry electrode was placed in the fourth intercostal space on the right chest near the sternum. The location is equivalent to the V₁ position in the standard 12-lead configuration. The Lead-I signal was measured using commercial 3M Ag/AgCl electrodes (T716) placed on the volunteer's left and right wrists, with the reference electrode on the left ankle. The ECG signals were digitally filtered in MATLAB by a 50th-order highpass filter with a cutoff at 0.5 Hz.

Supporting Information

Supporting Information is available from the Wiley Online Library or from the author.

Acknowledgements

This work was partially funded by NextFlex grant # 042299 and National Science Foundation Division of Civil, Mechanical and Manufacturing Innovation grant # 1635729. T.P. was partially supported by the IBM PhD fellowship. The authors thank Zhenghui Wu for his experimental assistance and helpful discussions.

Conflict of Interest

The authors declare no conflict of interest.

Keywords

electrophysiology, poly(3,4-ethylenedioxythiophene) polystyrene sulfonate, printing, stretchable dry electrodes

Received: May 1, 2017

Revised: June 13, 2017

Published online:

- [1] L. De Liao, C. T. Lin, K. McDowell, A. E. Wickenden, K. Gramann, T. P. Jung, L. W. Ko, J. Y. Chang, *Proc. IEEE* **2012**, *100*, 1553.
- [2] B. He, R. J. Cohen, *IEEE Trans. Biomed. Eng.* **1992**, *39*, 1179.
- [3] Y. Fukuoka, K. Miyazawa, H. Mori, M. Miyagi, M. Nishida, Y. Horiuchi, A. Ichikawa, H. Hoshino, M. Noshiro, A. Ueno, *Sensors* **2013**, *13*, 2368.
- [4] W. Besio, T. Chen, *Physiol. Meas.* **2007**, *28*, 515.
- [5] G. Prats-Boluda, L. Gil-Sanchez, Y. Ye-Lin, J. Ibañez, J. Garcia-Casado, E. Garcia-Breijo, *Proc. Eng.* **2012**, *47*, 1223.
- [6] R. A. Street, T. N. Ng, D. E. Schwartz, G. L. Whiting, J. P. Lu, R. D. Bringans, J. Veres, *Proc. IEEE* **2015**, *103*, 607.
- [7] S. L. Swisher, M. C. Lin, A. Liao, E. J. Leeftang, Y. Khan, F. J. Pavinatto, K. Mann, A. Naujokas, D. Young, S. Roy, M. R. Harrison, A. C. Arias, V. Subramanian, M. M. Maharbiz, *Nat. Commun.* **2015**, *6*, 6575.
- [8] J. Kim, W. S. Kim, *Sens. Actuators, A* **2016**, *238*, 329.

- [9] T. N. Ng, D. E. Schwartz, P. Mei, B. Krusor, S. Kor, J. Veres, P. Broms, T. Eriksson, Y. Wang, O. Hagel, C. Karlsson, *Sci. Rep.* **2015**, *5*, 13457.
- [10] T. N. Ng, D. E. Schwartz, P. Mei, S. Kor, J. Veres, P. Bröms, C. Karlsson, *Flexible Printed Electron.* **2016**, *1*, 15002.
- [11] M. L. Hammock, O. Knopfmacher, T. N. Ng, J. B.-H. Tok, Z. Bao, *Adv. Mater.* **2014**, *26*, 6138.
- [12] W. G. Besio, K. Koka, R. Aakula, W. Dai, *IEEE Trans. Biomed. Eng.* **2006**, *53*, 926.
- [13] G. Prats-Boluda, Y. Ye-Lin, J. Bueno-Barrachina, R. Rodriguez de Sanabria, J. Garcia-Casado, *Meas. Sci. Technol.* **2016**, *27*, 25705.
- [14] S. M. Lee, J. H. Kim, H. J. Byeon, Y. Y. Choi, K. S. Park, S. Lee, *J. Neural Eng.* **2013**, *10*, 36006.
- [15] C. T. Lin, L. De Liao, Y. H. Liu, I. J. Wang, B. S. Lin, J. Y. Chang, *IEEE Trans. Biomed. Eng.* **2011**, *58*, 1200.
- [16] J. J. S. Norton, D. S. Lee, J. W. Lee, W. Lee, O. Kwon, P. Won, S.-Y. Jung, H. Cheng, J.-W. Jeong, A. Akce, S. Umunna, I. Na, Y. H. Kwon, X.-Q. Wang, Z. Liu, U. Paik, Y. Huang, T. Bretl, W.-H. Yeo, J. A. Rogers, *Proc. Natl. Acad. Sci. USA* **2015**, *112*, 3920.
- [17] P. Leleux, J. M. Badier, J. Rivnay, C. Binar, T. Herve, P. Chauvel, G. G. Malliaras, *Adv. Healthcare Mater.* **2014**, *3*, 490.
- [18] M. R. Abidian, D. C. Martin, *Biomaterials* **2008**, *29*, 1273.
- [19] D. C. Martin, *MRS Commun.* **2015**, *5*, 131.
- [20] E. Bihar, T. Roberts, M. Saadaoui, T. Herve, J. B. De Graaf, G. G. Malliaras, *Adv. Healthcare Mater.* **2017**, *6*, 1601167.
- [21] J. Rivnay, S. Inal, B. A. Collins, M. Sessolo, E. Stavridou, X. Strakosas, C. Tassone, D. M. Delongchamp, G. G. Malliaras, *Nat. Commun.* **2016**, *7*, 11287.
- [22] M. Ramuz, A. Hama, M. Huerta, J. Rivnay, P. Leleux, R. M. Owens, *Adv. Mater.* **2014**, *26*, 7083.
- [23] S. H. Jeong, S. Zhang, K. Hjort, J. Hilborn, Z. Wu, *Adv. Mater.* **2016**, *28*, 5765.
- [24] O. Makeyev, W. Besio, *Sensors* **2016**, *16*, 858.
- [25] E. Huigen, A. Peper, C. A. Grimbergen, *Med. Biol. Eng. Comput.* **2002**, *40*, 332.
- [26] P. R. F. Rocha, P. Schlett, U. Kintzel, V. Mailänder, L. K. J. Vandamme, G. Zeck, H. L. Gomes, F. Biscarini, D. M. de Leeuw, *Sci. Rep.* **2016**, *6*, 34843.
- [27] J. Rubinson, Y. Kayinamura, *Chem. Soc. Rev.* **2009**, *38*, 3339.
- [28] M. E. Orazem, B. Tribollet, *Annu. Rev. Anal. Chem.* **2010**, *3*, 207.
- [29] J. Bisquert, G. Garcia-Belmonte, P. Bueno, E. Longo, L. O. Bulhões, *J. Electroanal. Chem.* **1998**, *452*, 229.
- [30] D.-H. Kim, N. Lu, R. Ma, Y.-S. Kim, R.-H. Kim, S. Wang, J. Wu, S. M. Won, H. Tao, A. Islam, K. J. Yu, T. Kim, R. Chowdhury, M. Ying, L. Xu, M. Li, H.-J. Chung, H. Keum, M. McCormick, P. Liu, Y. Zhang, F. G. Omenetto, Y. Huang, T. Coleman, J. A. Rogers, *Science* **2011**, *333*, 838.
- [31] A. J. Bandothkar, R. Nuñez-Flores, W. Jia, J. Wang, *Adv. Mater.* **2015**, *27*, 3060.